

Heat Transfer Coefficient Distribution of W and Broken W Turbulators At High Reynolds Numbers

Sam Ghazi-Hesami

Polytechnique Montréal
Montréal, Québec, Canada, H3T 1J4
sam.ghazi-hesami@polymtl.ca
(Siemens Energy Canada Ltd,
sam.ghazi-hesami@siemens-energy.com)

Dylan Wise

University of Oxford
Oxford, Oxfordshire, UK, OX2 0ES
dylanjaywise@gmail.com

Keith Taylor

Siemens Energy Canada Ltd
Montréal, Québec, Canada, H9P 1A5

Étienne Robert

Polytechnique Montréal
Montréal, Québec, Canada, H3T 1J4

Peter Ireland

University of Oxford
Oxford, Oxfordshire, UK, OX2 0ES

Abstract

An experimental and numerical study of the convective heat transfer enhancement provided by two rib families (W and Broken W) is presented, covering Reynolds numbers (Re) between 300,000 to 900,000 in a straight channel with a rectangular cross section ($AR=1.29$). These high Reynolds numbers were selected for the current study since most data in the available literature typically pertain to investigations at lower Reynolds numbers. The objective of this study is to assess the local heat transfer coefficient (HTC) enhancement (compared with a smooth channel) and the overall thermal performance, taking into account the effect of increased roughness on the friction factor, of a group of W shaped turbulators over a wide range of Reynolds numbers. Furthermore, the effects of increasing the rib spacing on the thermal performance of the Broken W configuration are presented and discussed. The numerical results are compared against heat transfer measurements obtained using the Transient Liquid Crystal (TLC) method.

The research shows that for the Broken W turbulators, increasing the Reynolds number is associated with an overall decrease of the thermal performance while the thermal performance of the W configuration is relatively insensitive to Reynolds number. Nevertheless, the Broken W configuration delivers higher thermal performance and heat transfer compared with the W configuration for the range of Re investigated. The Broken W configuration with a pitch spacing of 10 times the rib height was shown to provide the optimal thermal performance in the configurations investigated here.

1 Introduction

Improvements of heat exchanger thermal design, in electronic, solar and gas turbine industries are crucial for several modern applications. For instance, a gas turbine efficiency can be improved by increasing the combustion chamber temperature and consequently the turbine inlet temperature, requiring more cooling to protect the service life of sensitive components. In this example, the objective of a design engineer is to enhance the effectiveness of the cooling flow to allow more air to be directed to the combustion process. One method for improving surface heat transfer is through the use of surface features in the form of ribs. Rib roughened surfaces enhance heat transfer, compared with a smooth surface, by breaking the boundary layer, improvement of mixing and increase of surface area. However, introduction of turbulators and therefore additional surface area in a smooth channel also leads to increased surface friction and flow disturbance, which in turn increase pressure loss. This compromise can be quantified through the thermal performance of a surface, a measure of the improvement in heat transfer of a roughened versus a smooth channel, typically presented for a constant pumping power. What can be defined as the best turbulator configuration is application dependent, but the general intent is often to maximize the overall magnitude and spatial uniformity of heat transfer distribution over a surface while minimizing pressure loss. It is also important to consider manufacturability of such turbulators. However, recent developments especially in the field of additive manufacturing have enabled fabrication of complex geometries, whose thermal performance needs to be assessed.

The investigation presented here expands the available literature on high performance turbulators. W-shaped ribs were selected because they have shown promise to create complex 3D flow fields [1-5], useful for enhancing heat transfer but also representing a challenge for experimental and numerical studies, especially at elevated Reynolds numbers. The objective of the current investigation was to rank the turbulators considered and provide insight into the general flow characteristics by comparing the thermal footprint of the flow (from the liquid crystal experiments) and the numerically estimated pathlines. This comparative study provides an assessment of the effect of breaking the W rib as well as varying the broken rib spacing on turbulator performance. In the present investigation, turbulators were mounted only on one side of the test section (width).

A survey of the literature reveals that investigation of turbulator performance at high Reynolds numbers ($Re > 100,000$) has gained attention in recent years, with several examples available for gas turbine applications [1, 2, 4-8]. In the case of gas turbines, the need to improve the efficiency along with advances in manufacturing (e.g. additive manufacturing) have

likely encouraged investigations of cooling with complex-shaped turbulators in high Re regions such as the combustion chamber. As an example, Maurer et al. [4, 6] reviewed the need to improve turbulator heat transfer and minimize pressure loss for gas turbine combustors. The current study is complementary to other recent work addressing high Reynolds number convective cooling, where heat transfer and pressure loss were examined for Re up to approximately 400,000-550,000 [1, 2, 4-6, 8] and 1,300,000 [7]. Therefore, a unique combination of turbulator and test channel geometric parameters is experimentally examined to provide additional data points in the design space investigated by the previous authors. Numerical analysis is then performed to improve understanding of the flow features. As the majority of investigations available in the literature focus on low Reynold number ($Re < 100,000$) applications (e.g Ref [9-12]), the current study provides novel experimental data for rib cooling at high Reynolds numbers between 300,000 and 900,000. The hydraulic diameter of the current test section is 0.384 m, allowing for a large mass flow (and therefore Re) in the wind tunnel test section. The wind tunnel operates under atmospheric conditions and the flow remains incompressible as the Mach number remains under 0.3. Although the presented data is not intended for a specific application, it may be pertinent to a variety of high Reynolds number applications ($Re > 100,000$) such as gas turbine combustors.

In the following, a brief review of the literature is presented. This is followed by a description of the experimental facility, designed to cover the Re range spanning from 300,000 to 900,000. The results are then presented and discussed for W and Broken W ribs.

2 State of the Art

Following conventions found in the literature, in the following the rib height (e) and rib spacing (P) are normalized by the test channel hydraulic diameter (e/D_h ratio) and rib height (P/e ratio), respectively. A summary of the parameters and configurations, from the cited references, pertaining to W type ribs is outlined in Table 1.

2.1 Experimental Work

Aerothermal characteristics of turbulators have been studied in recent decades starting from simple parallel ribs to those with complex shapes [1-14].

Parallel ribs inclined at an angle relative to the duct axis were found to generally provide higher ribbed wall heat transfer coefficient (HTC) levels compared with parallel ribs set perpendicular to the flow [14-17]. This was attributed to the secondary flow induced by the angled ribs [14]. Han et al. [14] studied the effect of rib angle and channel aspect ratio ($AR=W/H$) for Reynolds numbers from 10,000 to 60,000 for channels with ribs on two opposite walls (over the channel width) in a narrow ($W/H<1$) rectangular cross section. They examined rib angles between 30° to 90° , concluding that the 60° ribs provided the highest heat transfer coefficient while the 45° ribs delivered the best thermal performance at constant pumping power in their experiments. However, the superior heat transfer augmentation of parallel angled ribs over transverse ribs was reported to deteriorate with an increase of the channel aspect ratio from $AR=1/4$ to 4 [14, 18, 19]. The potential interaction of the flow on the two opposite ribbed walls in these experiments was considered as a contributing factor to this trend, as the channel became wider and thinner [18, 19].

Several other studies have investigated the effect of more complex rib shapes, revealing superior performance for V and W ribs compared with parallel angled and transverse ribs over a range of channel aspect ratios [2, 3, 17, 20]. Additionally, W ribs were reported to provide improved heat transfer and thermal performance compared with V ribs [3, 4]. This implies better heat transfer can be obtained by increasing the number of V segments in a row to form a W rib.

The effect of rib spacing for W ribs was studied by Kunstmann et al. [2] and Maurer et al. [4], with the experimental data indicating a P/e ratio of 10 to be the optimum rib spacing for heat transfer augmentation and thermal performance, in comparison with P/e ratios of 5 [4] and 20 [2]. These studies were performed at Reynolds numbers between 80,000 and 500,000 in rectangular channels with an aspect ratio of 2 at e/D_h ratios of 0.06 [2] and 0.02 [4]. Although many studies investigated heat transfer on the surface between the ribs, Maurer et al. [6] showed a noticeable contribution of the rib heat transfer to the overall heat transfer of the ribbed surface.

An assessment of the effect of rib height for the W rib configuration showed an increase of the e/D_h ratio from 0.02 to 0.06 at a P/e ratio of 10 improves the heat transfer augmentation, at the expense of a large pressure penalty leading to a lower thermal performance [2]. Hagari et al. [1] assessed the thermal performance of short W ribs ranging from e/D_h ratio of 0.006 to 0.014 at Reynolds numbers between 40,000 and 550,000. They noticed the heat transfer augmentation and friction factor stabilizing at Reynolds numbers of approximately 300,000 and 50,000-100,000 respectively. Their study is interesting as it shows significant improvement of heat transfer augmentation can be obtained with very short W ribs, encouraging design engineers to consider smaller ribs due to their potential lower cost of manufacturing and reduced pressure loss.

The effect of breaking continuous ribs along their length, to form discrete surface features, was studied by Tanda [12], Wright et al. [20] and Han and Zhang [21]. These investigations indicated that discrete ribs provide superior heat transfer augmentation and thermal performance compared with continuous ribs, implying agreement with a hypothesis of enhanced generation of turbulence and secondary flows [21].

Table 1: Summary of parameters in investigations pertaining to W type ribs

Reference	Configuration	e/D_h	P/e	Re	Channel AR
Hagari et al. [1]	Ribs on one side	0.006-0.014	10	40K-550K	4.375:1
Kunstmann et al. [2]	Ribs on one side	0.02-0.06	10 & 20	130K-475K	2:1
Li et al. [3]	Ribs on one side	0.029	10	10K-60K	6:1
Maurer et al. [4]	Ribs on one side	0.02	5 & 10	80K-500K	2:1
Zhang et al. [5]	Ribs on two sides	0.1	10	150K-400K	1:1
Wright et al. [20]	Ribs on two sides	0.078	10	10K-40K	4:1

2.2 Numerical Studies

Flow fields and heat transfer patterns induced by surface mounted turbulators were also investigated numerically [1-4, 22-24]. Although computational methods are powerful tools for providing insight into complex aerodynamics, they require some form of validation to ensure reliable estimation of flow field characteristics and are therefore often compared against experimental studies. Maurer et al. [4] used a two-layer κ - ϵ turbulence model and reported a general underestimation of the Nusselt number distribution and friction factor in the numerical results, compared with the experimental data in their study of V and W ribs. This discrepancy, between the experimental data and the numerical estimates, grew with the increase of the P/e ratio from 5 to 10. Coincidentally, the numerical estimates predicted the formation of an additional vortex system with the increase in P/e ratio. Nevertheless, their numerical simulations proved valuable for the understanding of large flow structures and general flow characteristics. Li et al. [3] reported that the low-Reynolds number AKN κ - ϵ model [25] provides better agreement with the experimental data than the κ - ϵ Realizable and SST models. However, Tang and Zhu [24] and Chaube et al. [22] reported good agreement between numerical estimates, using the κ - ω SST model, and experimental data in their study of turbulators.

In the present investigation, the objective of the numerical analysis is to provide insight and qualitative characterization of dominant flow features, using the κ - ω SST turbulence model [26, 27] at high Reynolds numbers, to complement the experimental measurements. The numerical estimates are used for qualitative comparison of the flow pathlines with the experimentally measured HTC, providing a basis for the interpretation of the flow structures that drive heat transfer on the ribbed surface. Comparisons of numerically estimated flow features and the experimental data are performed and presented in Section 6. Additionally, recommendations are provided for a thorough validation of the numerical estimates.

3 Experimental Approach

3.1 Test Facility

The experiments were carried out in a new facility designed to achieve Reynolds numbers of up to 1,000,000. As shown in Fig. 1, the open-loop wind tunnel features a stainless-steel bell-mouthed inlet, including a flow straightener. The inlet reduces the area by a factor of 4 to the section where the heater mesh is located.

As described in Ireland et al. [28], presenting a similar facility, the heater mesh is made from stainless steel with a wire diameter of 40 μ m and aperture size of 63 μ m. It is soldered to two brass bars allowing electrical connections and electrically insulated from the wind tunnel structure using Tufnol®. The heater mesh is powered by a DC power supply capable of providing 150kW. As a safety feature, a flow sensing switch located in the diffuser section does not allow power to be supplied to the heater mesh if there is no air flow through the channel. Immediately following the heater mesh is an insulated transition section which is lined with a low-conductivity material (Rohacell®) to minimize heat loss from the fluid prior to entering the test section. The minimum distance between the heater mesh and the most upstream turbulator row in the test section is 4.35 times the hydraulic diameter (D_h).

Three walls of the test section are manufactured from wood (medium-density fibreboard) with the fourth wall being made up by a removable acrylic glass (poly methyl methacrylate) test plate, firmly clamped in position. The test plate is sprayed with thermochromic liquid crystal paint to allow a detailed HTC distribution to be calculated over the transparent area between the ribs.

Following the test section is an aluminium diffuser section which transitions to the blower inlet. The blower is powered by a 50 HP 3-phase induction motor with a maximum speed of 1460 rpm.

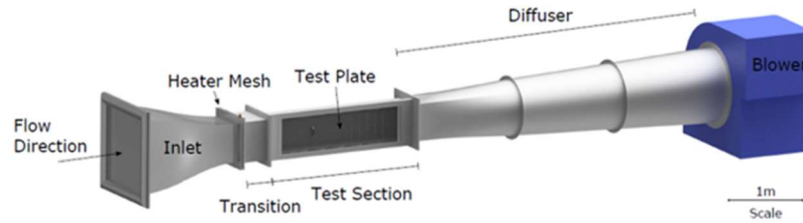


Fig. 1: Schematic representation of experimental facility

3.2 Liquid Crystal Measurements

Thermochromic liquid crystals have been used in heat transfer research since the early 1970's [29]. Details of the calculation method and further explanations of the liquid crystal technology and its benefits can be found in the literature [30].

Over the past two decades, the Transient Liquid Crystal (TLC) method has become a powerful experimental technique to measure high-resolution, steady-state HTC's. The technique uses thermochromic liquid crystal coatings applied to the surfaces where HTC's are sought [31]. Encapsulated cholesteric liquid crystals can be used to measure surface temperature for temperatures ranging from -30 to 150°C. Crystals typically used in experiments exhibit a full scale color change over a range of either 1°C, known as 'narrow band', or 20°C, known as 'wide band' [28, 30]. The narrow band crystals, color change over 1°C, are used in the current experiments. In their optically active phase, intermolecular forces cause adjacent layers of molecules to align themselves at a slight angle to each other, resulting in the thermochromic behaviour [28, 30].

The technique implemented here uses a step change in the gas temperature provided by the heater mesh to generate a heat flux into the test plate made from an insulating material, in this case, acrylic glass. This material is used here as it is transparent, allowing the liquid crystals, applied to the test plate surface exposed to the flow, to be monitored from the outside. Ireland and Jones [30], Ireland et al. [28] and Tsang [32] provide detailed information on transient liquid crystal methodology, the performance of the heater mesh and the liquid crystal response. In the inverse analysis used to determine the HTC's, the substrate is considered to be semi-infinite in thickness due to a shorter time for the liquid crystal color change compared with the time required for the thermal pulse to travel the thickness of the wall, as described by Ieronymidis et al. [10]. Known analytical one-dimensional solutions of Fourier's equation for heat conduction can then be used to extract HTC's from the surface temperature rise. The analysis requires knowledge of the initial temperature, gas and surface temperature

histories and the thermal properties of the substrate material and gas flow. The heat transfer coefficient can then be calculated via Eq. 1 (Tsang [32], Ireland and Jones [30], Clifford et al. [33]).

$$T_s = T_0 + (T_g - T_0) \left[1 - \exp\left(\frac{h^2 t}{\rho c k}\right) \operatorname{erfc}\left(\frac{h \sqrt{t}}{\sqrt{\rho c k}}\right) \right] \quad (1)$$

Where T_s , T_0 and T_g are surface temperature, initial temperature and gas temperature. Time is represented by “t” and $\sqrt{\rho c k}$ is the thermal product of the substrate and reported to be $569 \pm 29 \text{ W} \cdot \text{s}^{0.5} / (\text{m}^2 \cdot \text{K})$ for Perspex® [34].

The gas temperature is recorded with a minimally invasive fast response thermocouple on the centerline above the ribbed surface. As also discussed by McGilvray et al. [35], a mixed bulk value should ideally be used for the determination of the driving gas temperature. However, such measurements could not be performed in the current experimental set up without disrupting the flow field. The use of mixed bulk temperature for the determination of the HTC is especially advantageous in long channels [32]. Considering the short length of the channel, with only 5 rows of W ribs, the use of the centerline temperature is considered sufficient for the stated objective of the work presented here, that is to provide a comparative study and ranking of the turbulators. We however recommend that the most promising configuration be examined in a longer channel with additional measurements (e.g. mixed bulk temperature) in a future investigation. Using a conventional video camera, information about the surface temperature is recorded by imaging the surface of interest which is coated in liquid crystals.

The process of calculating the HTC from the raw data has been automated using a Matlab GUI [31]. This image treatment algorithm converts the liquid crystal response, using a calibration file, to HTC at each pixel location as described by Ryley et al. [36]. The uncertainty stemming from measurement instrumentation is calculated using each individual input error through a perturbation analysis. This uncertainty calculation is described by Byerley [37] with reference to the work of Moffat [38].

For the present research, overall uncertainties in HTC range from +/-9 to +/-10.7%, with the maximum value of +/-10.7% being derived from the following: 3.3% from the initial temperature, 3.3% from the temperature rise, 5.1% from the thermal product, 8.2% from the calibration and 0.4% from video time offset. The shorter time for liquid crystal color transition at high Re, leads to increased uncertainty. The friction factor measurement uncertainty is estimated to be within +/-4%.

3.3 Rib Heat Transfer Coefficient

As the TLC method is unable to establish the HTC values on the ribs themselves, another method was used to estimate the HTC at these locations. Although most ribs were made of acrylic glass, the inner segments of the ribs in the fourth downstream row (see Fig. 2) were made from brass and instrumented with thermocouples. These thermocouples were embedded into the rib segments and therefore are not on the turbulator surface. This allowed the use of the lumped capacitance method for the calculation of average HTCs.

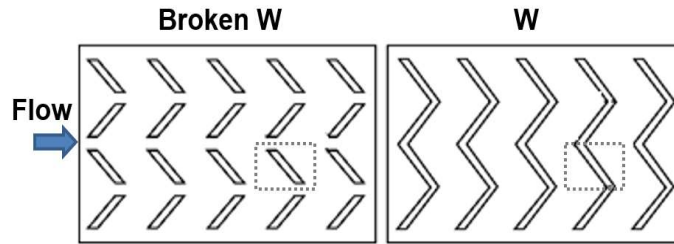


Fig. 2: Location of instrumented brass rib segments shown by dashed lines

The lumped capacitance method is a simple one-dimensional transient model that assumes that heat is convected between a fluid and a spatially uniform solid. As the temperatures are low, radiation effects are neglected. The brass ribs are thin (hollow) and glued to the plate, therefore ensuring minimal contact with the acrylic glass plate, reducing conduction. For this investigation, conduction is therefore neglected. Any conduction taking place will act to lower the brass temperature and reduce the calculated HTC so these calculations can be considered as conservative.

In order to apply the lumped capacitance method, the Biot (Bi) number must be typically $Bi < 0.1$ [39]. The Biot number is based on the heat transfer coefficient (HTC), material conductivity (k) and the rib characteristic length (L_c). The largest heat transfer coefficient measured during the experiments is of the order of $h \approx 300 \text{ W/(m}^2\text{.K)}$, the conductivity of brass is $k \approx 109 \text{ W/(m.K)}$. This results in a Biot number of $Bi = 0.032$ which implies that the temperature gradients within the solid are negligible [40]. The transient temperature response can then be determined by applying an overall energy balance to the solid. This is shown in Eq. (2), where the left-hand side refers to the rate of heat transfer at the surface due to convection and the right-hand side corresponds to the rate of change of internal energy.

$$-hA_s(T - T_\infty) = \rho V c \frac{dT}{dt} \quad (2)$$

T_∞ and T are measured by thermocouples and Eq. (3) is solved numerically, allowing the HTC to be determined by regression.

$$T_{n+1} = T_n - \left[\frac{hA_s(T_n - T_\infty)}{mc} \right] dt \quad (3)$$

3.4 Rib Configurations

Two rib configurations were selected for this investigation including the well documented ‘W ribs’. This configuration has been studied extensively and data is available in the literature for heat transfer and friction factor measurements up to $Re \approx 500k$ [1, 2]. As mentioned previously, superior performance is expected for angled ribs, compared with parallel transverse ribs [14-17]. A 60° continuous W-shaped rib, shown in Fig. 3(a), was investigated and used as a baseline configuration.

The performance of discrete ribs compared with continuous parallel angled or V-shaped ribs are reported to be superior in most channels [16], motivating our investigation of a ‘Broken W configuration’ at high Reynolds numbers. Therefore, to further increase the heat transfer performance, the W configuration was broken along the length to form the Broken W configuration (Fig. 3(b)). Broken configurations are thus interrupted in one or more locations, so the ribs are no longer continuous. All turbulators represent an obstacle at a 60° angle relative to the main flow and the ribs have a square cross section. For both rib configurations, five successive turbulator rows were placed on the test plate. The test section (Fig. 1) is 2 m long and the ribs are placed on one side of the channel. The experimental set up for the W rib turbulator configuration is illustrated in Fig. 4, however a similar arrangement was used for the broken W configurations. The width and height of the test section are 0.44 m and 0.34 m ($AR=1.29$) respectively. The rib pitch is 0.116 m and the size of the gap between the turbulator and the sidewall (Fig. 4(b)) is 7.56% of the channel hydraulic diameter.

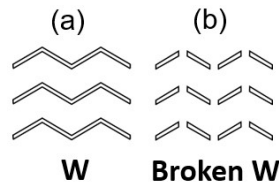


Fig. 3: Rib configurations, W (a) and Broken W ribs (b)

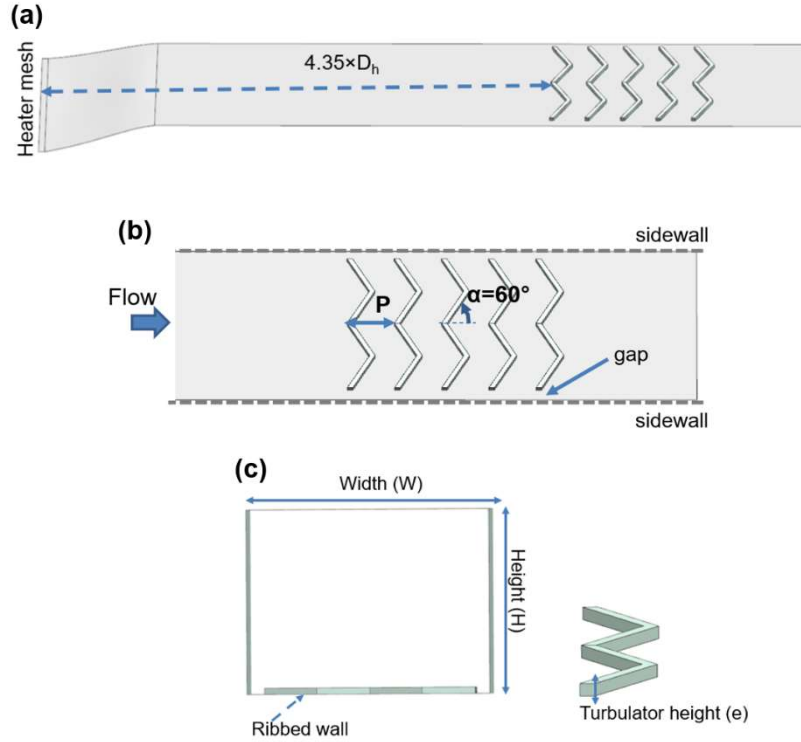


Fig. 4: Duct configuration (a) turbulator configuration (b) test channel cross section and turbulator height (c)

The nominal relative height for all configurations tested was set at $e/D_h = 0.03$. The nominal pitch was set at $P/e = 10$, although two other pitches were tested for the Broken W case to investigate the influence of pitch at high Reynolds numbers. Four plate configurations (with $e/D_h = 0.03$) were therefore tested in total and the details are presented in Table 2.

Table 2: Turbulator configurations

Case	Type	P/e	Re	Channel AR	e/D_h
1	W	10	$300,000 \leq Re \leq 900,000$	1.29	0.03
2	Broken W	10	$300,000 \leq Re \leq 900,000$	1.29	0.03
3	Broken W	16	$300,000 \leq Re \leq 900,000$	1.29	0.03
4	Broken W	8	$300,000 \leq Re \leq 900,000$	1.29	0.03

3.5 Data Reduction

A pitot-static probe aligned with the centerline of the test section allows the flow velocity (v) to be determined. The Reynolds number is calculated using the following expression;

$$Re = \frac{\rho v D_h}{\mu} \quad (4)$$

Viscosity (μ) is calculated using the two coefficient Sutherland's law based on the centerline temperature. Density (ρ) is calculated using the ideal gas law. All Reynolds numbers specified are based on the test section hydraulic diameter (D_h).

To enable a performance comparison without the influence of sidewalls, a nominal area was considered in the middle of the test plate, corresponding to the dashed area of Fig. 5, for the calculation of average HTC. This region was chosen to begin at the leading edge of the 4th rib row and to extend in the flow direction exactly one row pitch. HTC's were not averaged over the areas corresponding to the 3 upstream rows as their purpose was to initiate and develop the turbulator secondary flows. To minimize wall effects, the considered area focused on the two central ribs, as seen in Fig. 5. The average HTC values are area weighted combinations of the surface HTC and the rib HTC. The average HTC values calculated for the ribs were applied to their base surface area for the overall average HTC calculations. The locations of the centerline thermocouple over the ribs and pressure probes are also illustrated in Fig. 5.

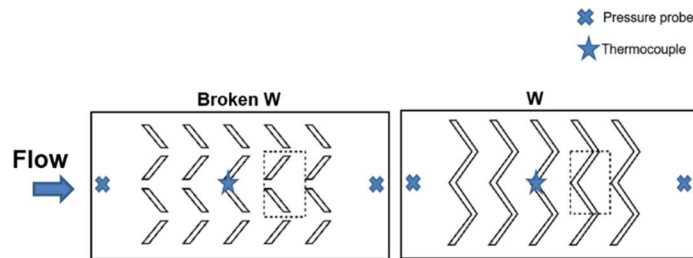


Fig. 5: Nominal area for HTC averaging (dashed area)

The HTC augmentation relative to a smooth wall was calculated by normalizing the experimental HTC values by the heat transfer coefficient calculation (Eq. (5)) using the fully developed smooth duct Dittus-Boelter correlation (Eq. (6)). The parameter “ k ” in Eq. (5) represents the air conductivity at the temperature measured by the thermocouples. Since the Dittus-Boelter correlation represents heat transfer with respect to the fluid mean bulk temperature in a long channel with fully developed flow, care needs to be exercised in directly comparing the HTC results of the current experiment with that of the

Dittus-Boelter correlation. In the current work, the centerline temperature is used, and the normalization of the experimental data (using the Dittus-Boelter correlation) is provided to improve the clarity of the data.

$$h_0 = \frac{Nu_0 k}{D_h} \quad (5)$$

$$Nu_0 = 0.023 Re^{0.8} Pr^{0.4} \quad (6)$$

Static pressure measurements were made at the centerline before and after the ribbed section to calculate the relative pressure drop. The friction factor was then calculated using the following equation.

$$f = \frac{(\Delta p / \Delta x) D_h}{2 \rho v^2} \quad (7)$$

The friction factors were normalized by the friction factor for fully developed flow in a smooth tube using the relationship developed by Blasius to yield Eq. (8).

$$f/f_0 = \frac{f}{0.046 Re^{-0.2}} \quad (8)$$

A simple performance parameter, known as thermal performance, was used to combine heat transfer augmentation and friction factor to give an overall value for the use of ribbed walls for heat transfer augmentation, as described by Fan et al. [41]. The method is based on heat exchanger performance at constant pumping power. The performance parameter is calculated using Eq. (9).

$$\eta_T = \frac{h/h_0}{(f/f_0)^{2/7}} \quad (9)$$

4 Numerical Simulation

The flow characteristics of W and Broken W ribs are also investigated numerically, for $P/e=10$ and $e/D_h 0.03$, using a Reynolds-Averaged Navier-Stokes (RANS) model ($\kappa\text{-}\omega$ SST) in ANSYS Fluent® 17.1. The $\kappa\text{-}\omega$ SST model draws on the strengths of the $\kappa\text{-}\omega$ turbulence model for the characterization of the flow near the wall while relying on the $\kappa\text{-}\epsilon$ model away from the wall, to form a hybrid approach [26, 27]. This RANS model is selected due to its successful use in turbulator aerodynamic investigations, such as those by Chaube et al. [22] and Tang and Zhu [24].

Attempts at generating grids for the entire wind tunnel geometry demonstrated that tens of millions of elements would be needed for the numerical results to achieve grid independence, even if the overall channel flow and target ribbed segments were meshed and simulated separately, similar to the work of Hagari et al. [1]. Therefore, here only one fully translationally periodic segment, covering a full rib pitch, is simulated to reduce computational cost. The numerical simulations are performed at Reynolds number of 903,000 and 908,000 for the W and Broken W configurations, respectively. This operating condition was selected because high Reynolds number is expected to yield the highest velocity gradients and flow disturbance. Although, this numerical approach may not provide a thorough quantitative characterization of the flow field for the current experiments, it can offer general qualitative insight into key flow attributes, such as the location of large flow structures and the relative spatial distribution of Turbulent Kinetic Energy (TKE). Areas of near wall augmented TKE are reported as an indication of enhanced mixing and improved heat transfer [3, 24], providing a basis for the interpretation of the numerical results generated here and their comparison with our experiments. As a result of this limited computational domain, the numerical results cannot be quantitatively compared against the experiments. This is due to the assumption of perfect periodicity made in the numerical simulations which cannot be confidently postulated for the experiments, due to the limited number of turbulator rows. A full wind tunnel simulation using RANS and LES turbulence models (similar to the work of Lörstad [23]) is recommended in a future investigation for comparison against the current experimental data and detailed assessment of numerical approaches.

4.1 Boundary Conditions

One segment (equivalent to one pitch) of the W and Broken W configurations was modelled, as shown in Fig. 6. Further reduction of the computational domain was obtained by using a symmetry boundary condition at the center of the W rib. The inlet and outlet boundaries were made periodic with a defined mass flow rate boundary condition and no-slip

boundary conditions were applied on the walls. Isothermal wall condition with a fixed temperature was assigned to the ribbed wall and adiabatic boundary conditions were assumed for all the other walls. The SIMPLE algorithm was used for pressure-velocity coupling and spatial discretization was performed using a second order upwind scheme for momentum, energy, TKE and specific dissipation rate while a second order method was used for pressure. The incompressible ideal gas law (density as a function of temperature and operating pressure) was assumed for air since the wind tunnel Mach number does not exceed 0.2. Other fluid properties were calculated through linear relations, which were considered adequate due to the small overall temperature variation, $\Delta T \approx 15^\circ\text{C}$ between the wall and the heater mesh air temperatures.

4.2 Mesh Generation

A minimum of 10 inflation layers were applied on the walls with a smooth growth of aspect ratio from the cells immediately next to the wall to the outer region of the inflation layers (Fig. 7). Boundary layer refinement was performed to achieve $y^+ \approx 1$, resolving the viscous sublayer, to ensure proper estimation of near wall flow characteristics and heat transfer. Grids were generated using the CutCell algorithm with the ANSYS meshing tool. A mesh sensitivity analysis was performed to ensure solutions were independent of grid resolution. Grids with 3.61 million, 7.75 million, 22.87 million, 26.12 million, 35.04 million, 45.9 million and 58.2 million elements were created for the Broken W configuration. The W configuration was meshed with 4.04 million, 27.83 million and 35.29 million elements. Negligible discrepancies of area averaged heat transfer, pressure drop and velocity profile were observed between the two largest grids for both models. Therefore, numerical estimates are presented using the 45.9 million element grid for the Broken W geometry and 27.83 million element grid for the W geometry. Normalized error residuals as well as relevant quantities (velocity profile, heat transfer coefficient and pressure drop) were monitored, to assess solution convergence, until these parameters showed stability with additional iterations.

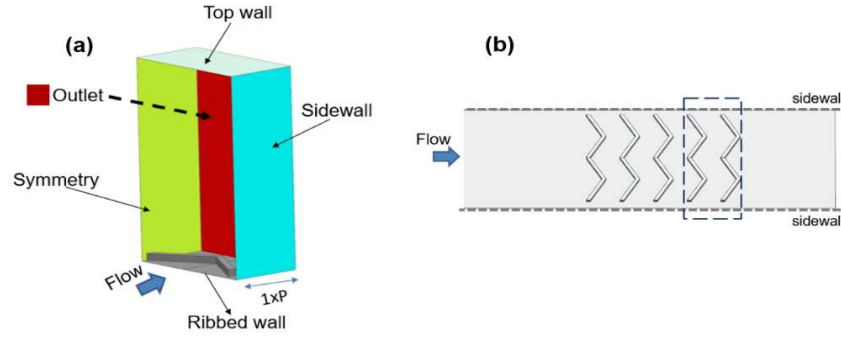


Fig. 6: Numerical domain, shown for the W configuration (a) and the corresponding area (shown by the dashed lines) in the experiment where HTC measurements are compared with the numerically estimated flow structures

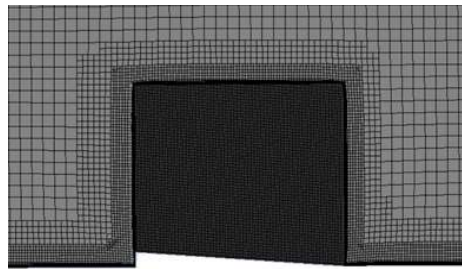


Fig. 7: Mesh around rib

5 Experimental Results and Analysis

5.1 HTC of W and Broken W ribs

Normalized HTC, divided by HTC calculated using the Dittus-Boelter correlation, contours for both configurations ($P/e=10$) at the highest Reynolds numbers investigated are presented in Fig. 8 and Fig. 9, respectively. The thin line extending from the fourth turbulator (shown by the dashed arrows in Fig. 8 and Fig. 9) to the sidewall is a result of the localized optical noise caused by the thermocouple wire through the Perspex® plate and can be ignored as it has little effect on the overall heat transfer measurements. For all the Reynolds numbers tested, the HTC pattern remained qualitatively similar, with increasing magnitudes associated with increasing Reynolds number. From the figures, the flow disruption by the ribs is clearly visible, creating areas of low and high HTC through the separation and reattachment of the boundary layer. Moreover, the Broken W configuration is generating higher HTC values behind the ribs. This is consistent with

information found in the literature, albeit for lower Reynolds numbers, stating that interrupted ribs generally outperform continuous configurations.

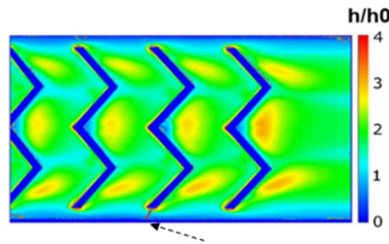


Fig. 8: Normalized HTC contour for W configuration at $Re=903k$ and $P/e=10$

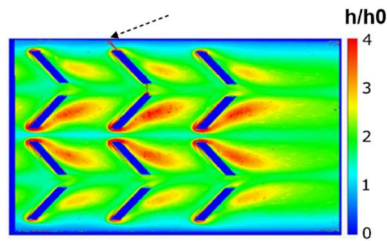


Fig. 9: Normalized HTC contour for Broken W configuration at $Re=908k$ and $P/e=10$

By calculating average HTC values over the areas shown in Fig. 5, a quantitative comparison between the two configurations can be made. Note that the averaged HTC values include heat transfer over the regions described in sections 3.3 and 3.5.

Figure 10 shows a comparison of average HTC (including the ribs) over the full range of Reynolds numbers measured experimentally. The averaged HTC values increase continuously and monotonically with increasing Reynolds number for both configurations. The Broken W configuration shows an approximately 20-30% improvement over the continuous W configuration over the range of Reynolds numbers from 300,000 to 900,000. The vertical bars in Fig. 10 demonstrate the aforementioned estimated experimental uncertainty, however these bars will not be replicated in the following plots for enhanced clarity of the plots.

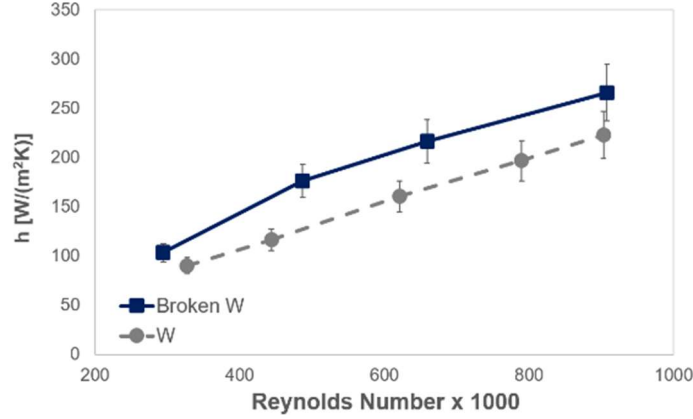


Fig. 10: Average HTC variation as a function of Reynolds number for the W and Broken W configurations ($P/e=10$)

The HTC augmentation of both configurations, with the same rib spacing, relative to the smooth duct correlation (Dittus-Boelter) is shown in Fig. 11. At low Reynolds numbers, the W configuration increases the HTC by a factor of 2.5 and this enhancement grows to approximately 2.75 at $Re \approx 900,000$. As expected, the Broken W configuration shows a greater HTC augmentation, ranging between 3 and 3.5 times the value obtained from the smooth duct correlation. The heat transfer augmentation of the W configuration, shows a slight increase with Reynolds number, contrary to the trends presented by Maurer et al. [4], Maurer et al. [6] and Wright et al. [20]. Although the heat transfer augmentation (including combination of rib and surface between successive ribs) presented by Maurer et al. [6] does not show a consistent decline with increasing Re , the overall trend indicates a declining heat transfer augmentation between the lowest and the highest Re . This may be due to the differences in the e/D_h ratio, channel length/aspect-ratio, orientation of the W shaped rib with respect to the inlet flow and the rib/sidewall gap in the current experiment. Additionally, the V segments of each discrete W rib of Ref [20] are axially staggered while the V segments are aligned between rows in the current investigation (Fig. 3(b)). For comparison the heat transfer augmentation for the current experiment is shown against the experimental data from Maurer et al. [6] in Fig. 12 at a similar P/e ratio. For consistency with the cited references [3, 6], heat transfer augmentations are presented in terms of Nusselt number (Nu) ratios. The overall Nu ratio [3] at lower Re is also presented (Fig. 12) for the W configuration and an extrapolated trendline is also included based on the current experimental data for the continuous W rib. The W rib data is used for the extrapolation as it may provide a better comparison with the literature [3, 6] due to its continuous structure. However, the relation between heat transfer augmentation and Re is not necessarily represented by the trendline and experiments at lower Re are required to confirm this observation. The comparison in Fig. 12 provides a general overview

and care must be taken in interpreting and comparing the data considering the differences such as the geometrical configuration and dimensions, channel length, Re , measurement and normalization of experimental data.

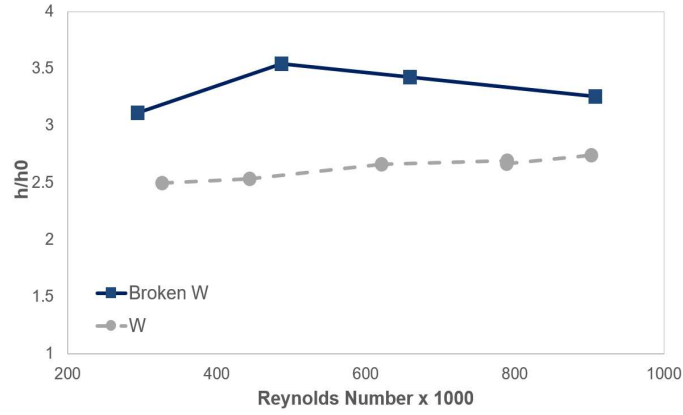


Fig. 11: Normalized average HTC variation with Reynolds number for the W and Broken W configurations ($P/e=10$)

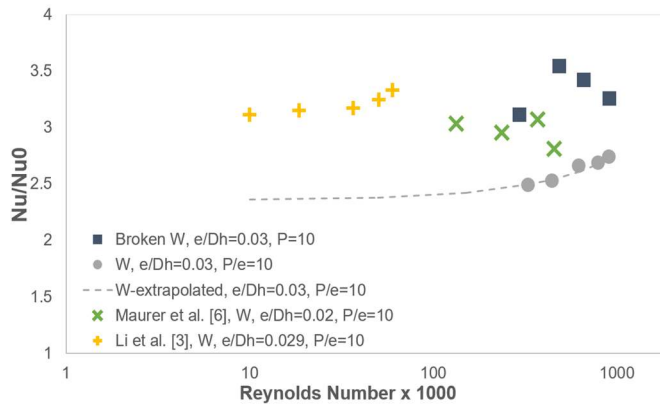


Fig. 12: Comparison of the heat transfer augmentation variation for the W and Broken W configurations ($P/e=10$) with the literature

5.2 Effect of the Rib Pitch on the HTC for Broken W ribs

As previously discussed, experimental data found in the literature indicate that for continuous W ribs a P/e ratio of 10 is the optimum rib spacing in a rectangular channel [2, 4]. For the current investigation, P/e ratios of 8, 10 and 16 were considered for the Broken W configuration to verify whether a P/e ratio of 10 also delivers the best performance over a wider range of Reynolds numbers for non-continuous ribs.

Figure 13 shows the normalized HTC distribution for the Broken W case at three pitch spacings, $P/e=8, 10, 16$. Both $P/e=8$ and $P/e=10$ show large HTC augmentation areas following the ribs, with the peak values at approximately 4 times the baseline smooth duct HTC. These areas are large and spread almost until the following rib. However, the high HTC areas following the ribs in the $P/e=16$ case are much smaller and only reach a maximum of approximately $h/h_0=3$.

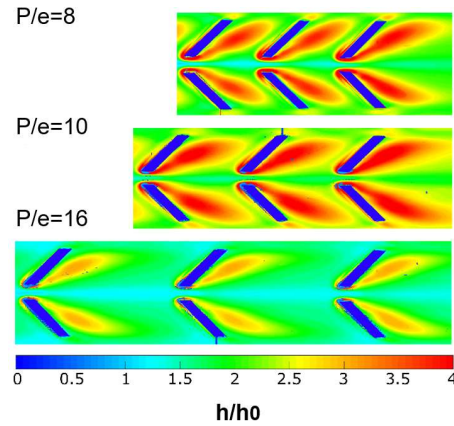


Fig. 13: Normalized HTC contours for different rib spacings of the Broken W rib configuration

To compare the performance of each case, area averaged normalized HTC values were calculated using the areas shown in Fig. 5. It can be seen from Fig. 14 that the $P/e=16$ case has the lowest HTC augmentation performance with the average h/h_0 values remaining approximately constant with Re , staying within 2.2 to 2.4.

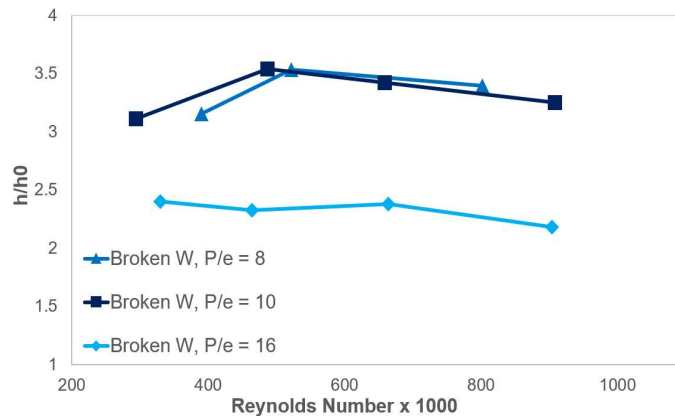


Fig. 14: Normalized HTC variation for the Broken W configuration at various rib spacings

Both the $P/e=8$ and $P/e=10$ cases perform almost identically, reaching a peak averaged $h/h_0=3.5$ at $Re \approx 500,000$. At lower Reynolds numbers, the heat transfer augmentation appears to significantly decrease while for $Re > 500,000$ this augmentation deteriorates slowly with increasing Re , reaching $h/h_0=3.25$ at $Re=900,000$.

5.3 Pressure Loss

Figure 15 shows the normalized friction factor for each of the four cases considered. First, it can be observed that at $P/e=10$, the W configuration produces a larger pressure drop than the Broken W, with a difference in the friction factor f/f_0 of approximately 15 to 20%. The broken configuration allows a portion of the flow to remain relatively undisturbed which may contribute to lower pressure drop. Accordingly, the broken rib configuration outperforms the continuous one in heat transfer augmentation and it also does so with less pressure drop.

Having established that the Broken W configuration performs better overall, we will now look at how the pitch spacing affects the pressure drop. Figure 15 shows that there is a clear trend of lower pitch spacing leading to a higher pressure drop. At Reynolds numbers approaching 1,000,000 the friction factor ratios for the $P/e=8$, $P/e=10$ and $P/e=16$ cases are 8.7, 7.1 and 5.8 respectively. These levels confirm the dramatic effect of pitch spacing on the pressure loss. However, as the flow may not be fully developed with the current set up, a longer domain with additional measurements may be required for improved insight.

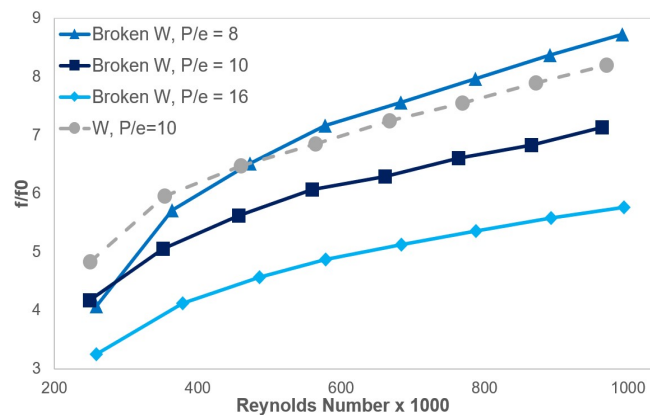


Fig. 15: Normalized friction factor for all four rib configurations investigated

5.4 Thermal Performance

To compare the configuration in terms of both heat transfer augmentation and pressure loss, the thermal performance parameter (η_T) given in Eq. (9) is calculated for a constant pumping power. Figure 16 plots the thermal performance as a function of Reynolds number for the four configurations considered.

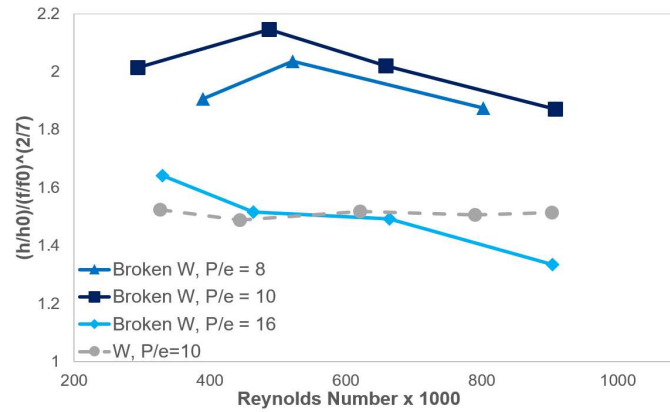


Fig. 16: Thermal performance of all four rib configurations investigated

The Broken W configuration has higher HTC augmentation and lower pressure loss, it therefore has a higher thermal performance than the continuous W configuration. The thermal performance of the two Broken W configurations with the shorter pitch peak at approximately $\eta_T = 2.10 \pm 0.05$, corresponding to a Reynolds number close to 500,000. As the Reynolds number increases further, HTC augmentation is slightly lower and the pressure loss increases rapidly. These two effects combine to result in a thermal performance which decreases with increasing Re.

With increasing Re, the continuous W configuration shows a slightly increasing HTC augmentation and a rapidly increasing pressure loss. Due to the dominant role of the HTC augmentation in the calculation of thermal performance at constant pumping power, the result is a nearly constant $\eta_T = 1.5$ across the Reynolds number range investigated. These results are interesting as they demonstrate an average thermal performance improvement of approximately 33%, obtained by breaking the continuous W turbulator, at P/e=10, along its length.

The effect of pitch spacing on the thermal performance of the Broken W configuration is also clear from Fig. 16. Although the P/e=8 case showed a similar HTC augmentation to the P/e=10 case, the increased pressure loss associated with increasing Re for more highly stacked ribs reduces the overall thermal performance. Although the P/e=16 case showed a lower pressure loss it was not enough to overcome the reduced heat transfer augmentation. The thermal performance of

the $P/e=16$ case is significantly lower than for $P/e=10$. This result is therefore consistent with the experimental data of Kunstmann et al. [2] and Maurer et al. [4] for continuous W ribs, showing that the optimum rib spacing is approximately $P/e=10$. In summary, the current experiment indicates feasibility of achieving thermal performance (>1) at elevated Reynolds numbers. However, evaluation of the thermal performance with additional turbulator rows in a longer channel is recommended to complement the current experiment.

Figure 17 shows a comparison of the thermal performance for the W and Broken W ribs at $P/e=10$ with the works of Li et al. [3] and Maurer et al. [4]. For consistency, the thermal performance in Fig. 17 is calculated similarly to the cited references [3, 4], where the friction factor ratio exponent is $1/3$. This is different than the exponent used in Eq. 9 and Fig. 16. The illustration of thermal performance values from the literature in Fig. 17 provides a general overview and care must be taken in interpreting and comparing the data considering the differences such as the geometrical configuration and dimensions, channel length, Re , measurement and normalization of experimental data. A review of Fig. 17 however indicates that the Broken W configuration appears to exhibit superior thermal performance compared with the continuous W configurations at high Re .

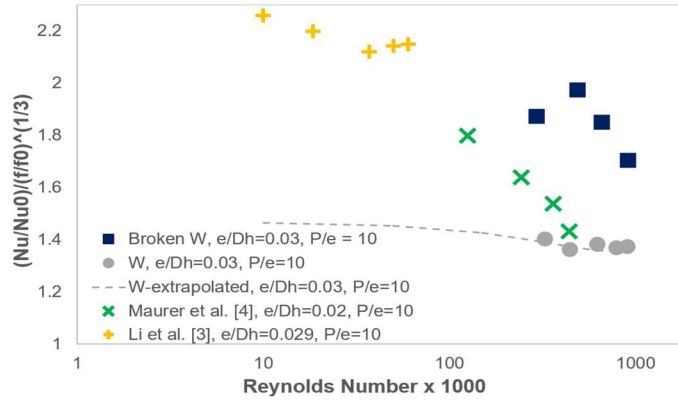


Fig. 17: Comparison of thermal performance of W and Broken W configurations at $P/e=10$ with the literature

6 Numerical Results and Discussion

In this section, the flow field disturbance caused by the ribs is discussed based on numerical simulation of the flow pathlines and normalized TKE, compared against the experimentally obtained normalized HTC distributions. Combined

CFD and high-resolution TLC data provide key understanding of the mechanisms leading to heat transfer augmentation and pressure loss.

To facilitate the discussion, three zones are defined around the fourth rib row, shown in Fig. 18 and Fig. 19, where the secondary tangential flow is established. Experimental normalized HTC (h/h_0) contours on the three most downstream ribs are illustrated in Fig. 19 with the dashed boxes indicating the three zones used for discussion. In Fig. 20, the flow pathlines on the ribs and in the inter-rib regions, for the W (frame a) and the Broken W (frame c) configurations are shown. The second frame for each case only shows the streamlines around the ribs, to highlight the secondary flow they generate. Figure 21((c) & (d)) reveal the spatial distribution of the normalized TKE in a plane (TKE contour normalized by the maximum TKE in this plane) normal to the flow, at $0.2x_P$ downstream of the rib apex. The dashed arrows in Fig. 21((c) & (d)) indicate the overall corresponding regions between the experimentally measured normalized HTC and the numerically estimated normalized TKE. In the absence of a large number of turbulator rows in the experiment to ensure fully periodic flow, the simulation estimates are compared within the dashed region in Fig. 21((a) & (b)). In general, as the flow reaches the turbulators, it is guided in the tangential direction due to their angle relative to the flow. The four legs of the W and Broken W configuration divert the local flow from the vicinity of the sidewalls and the symmetry line towards the apexes of the W configuration (pointing downstream), leading to tangential secondary flow streams, shown in Fig. 20.

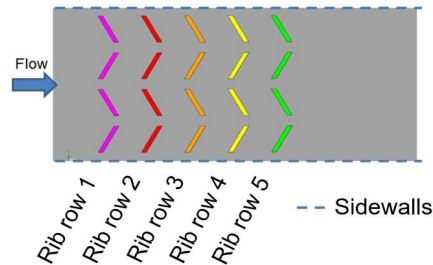


Fig. 18: Rib row numbering

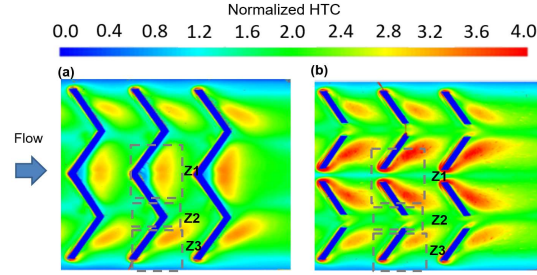


Fig. 19: Normalized HTC measured experimentally for the most downstream ribs at $Re=903,000$ (left) and $Re=908,000$ (right), with the 3 zones, shown by dashed boxes, used for the discussion of numerical results

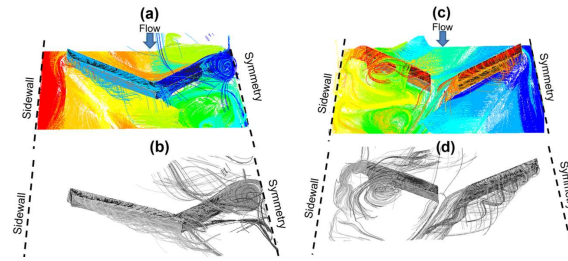


Fig. 20: Pathlines on the W configuration (a and b) and Broken W configuration (c and d) with the colors intended for improved visualization

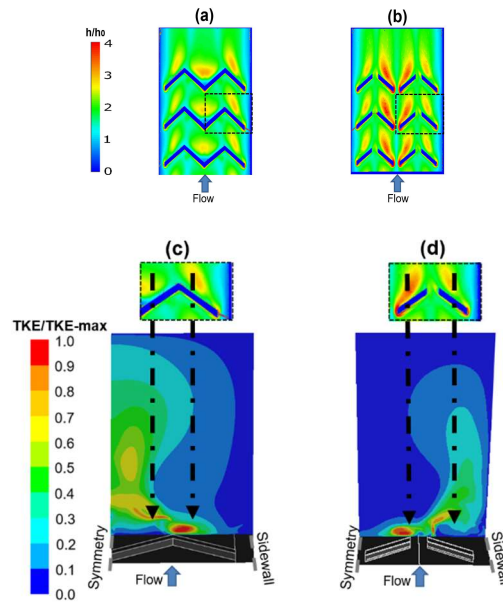


Fig. 21: Experimental normalized HTC on the most downstream ribbed segments (a & b) and numerically estimated normalized TKE at $0.2xP$ downstream of the apexes of W and Broken W ribs (c & d)

6.1 Zone 1

For the W configuration, a compact and wide area of peak heat transfer is observed shortly downstream of the rib in Zone 1 (Fig. 19(a)). Heat transfer improves at the point of flow re-attachment after it passes the upstream apex of the rib but deteriorates further downstream as the boundary layer grows in thickness.

The normalized HTC distribution for the Broken W configuration indicates that the flow passes without significant disturbance near the centerline between the two central rib segments, on the symmetry plane (Fig. 19(b)). This is confirmed by the pathlines of Fig. 20(c). However a large and intense vortical structure emanates from the edge of the rib segment near the symmetry line (Fig. 20(c) & (d)), the imprints of which can be observed in Fig. 19(b) by an area of peak heat transfer. Figure 21(d) shows an area of elevated normalized TKE near the ribbed surface corresponding to this region of increased heat transfer. The flow swirl, increased turbulence intensity and developing boundary layer likely contribute to the extended area of peak heat transfer in this region, similarly to the heat transfer mechanism of longitudinal vortices described by Fiebig [42, 43]. These results demonstrate that breaking the ribs increases the local heat transfer by inducing additional vortical structures and turbulence, as postulated by Han and Zhang [21].

6.2 Zone 2

Experimental data (Fig. 19) do not show a significant heat transfer improvement in this region near the downstream apex of the ribs, for both the W and Broken W configurations. The pathlines (Fig. 20) reveal relatively smooth flow without large vortical structures. For the broken W configuration, a smaller area of elevated normalized TKE, compared with zone 1, is observed in Fig. 21 downstream of the ribs and adjacent to the surface corresponding to Zone 2. It is suspected that the converging configuration of the rib segments in this area may lead to the destructive interaction of the secondary flow streams. This interaction may cause the dissipation or weakening of the near ribbed-wall vortex structures resulting in an area of lower heat transfer, compared with Zone 1, which does not considerably improve when a slit is introduced for the Broken W configuration. In a similar scenario for the comparison of V and reversed V configurations, the convergent legs of the reversed V configuration led to an area of reduced heat transfer which was attributed to the likely interference of the two counter rotating vortices [17]. This theory may be further examined by increasing the space between the rib segments (currently 7.56% of channel hydraulic diameter) of the Broken W, to study the effect of lateral rib element spacing on the heat transfer of the obstacles downstream.

6.3 Zone 3

For the W configuration, a longitudinal vortex starting from the extremity of the rib (near the sidewall) produces an elongated area of increased heat transfer downstream of the rib, as seen by comparing Fig. 19(a) to the streamlines of Fig. 20(a). The flow adjacent to the wall follows a nearly smooth path and provides little heat transfer augmentation in close proximity to the sidewall.

For the Broken W configuration, Zone 3 shows a smaller and more downstream area of peak normalized HTC, compared to zone 1. This may be partially attributed to the interaction of the trailing vortices with the boundary layer of the sidewalls. Figure 21(d) reveals lower intensity of normalized TKE near the ribbed wall in this region, compared with Zone 1. However, comparing Fig. 21((c) & (d)), shows that the higher normalized TKE region in the bulk flow has shifted from the center of the plate towards the sidewall as a result of the vortical structures and velocity gradients induced by the slits of the Broken W configuration.

For both configurations, uninterrupted boundary layer growth results in low heat transfer in close proximity of the sidewalls, where the distance between the rib and the sidewall is equal to 7.56% of the channel hydraulic diameter. This region of low heat transfer thins slightly in regions adjacent to the ribs, as seen in Fig. 19, as a result of the reduced effective area and local flow acceleration.

7 Conclusion

The experimental results presented reveal the thermal performance of two rib-type turbulator families (W and Broken W) at very high Reynolds numbers of up to 900,000. High-resolution heat transfer measurements were performed using the transient liquid crystal thermography technique, providing detailed HTC contours of the measured surfaces. This investigation showed that the Broken W case outperformed the continuous W case in terms of both heat transfer coefficient and pressure loss. Finally, the investigation shows that for the Broken W case, the optimum rib pitch to height ratio is $P/e=10$ for increased thermal performance at fixed pumping power. The thermal performance for all configurations was above 1, indicating all the examined W shaped turbulators deliver higher heat transfer compared with a smooth channel at a given pumping power.

The experimental results are compared against a numerical analysis, realized using the $\kappa\text{-}\omega$ SST turbulence model, providing qualitative insight into dominant flow characteristics. The numerical estimates indicated that breaking the rib near

the symmetry line leads to longitudinal vortical structures emanating from the corners of the rib legs. The same vortical structure was not observed in the converging (pointing downstream) legs of the Broken W rib, despite the slit introduced.

Acknowledgement

The authors are grateful to Siemens Energy Canada Limited for supporting this research and the permission to report this investigation. Thanks also go to Dr Andrew Dann, Dr James Turner and Dave Mountain for their contributions to the experimental work. Additionally, the authors thank all their colleagues who have helped with this investigation. Computing resource at Polytechnique Montréal was kindly supported via NSERC Discovery Grant RGPIN-2014-03622.

Permission for Use

The content of this paper is copyrighted by Siemens Energy Canada Limited and is licensed to ASME for publication and distribution only. Any inquiries regarding permission to use the content of this paper, in whole or in part, for any purpose must be addressed to Siemens Energy Canada Limited directly.

Nomenclature

A_s	[m ²]	surface area
c	[J/(Kg.K)]	specific heat capacity
D_h	[m]	hydraulic diameter
e	[m]	rib height
f	-	friction factor
f_0	-	smooth channel friction factor
H	[m]	channel height
h	[W/(m ² .K)]	heat transfer coefficient
h_0	[W/(m ² .K)]	smooth duct heat transfer coefficient
k	[W/(m.K)]	thermal conductivity
m	[Kg]	mass
Nu	-	Nusselt number
P	[m]	rib pitch

Pr	-	Prandtl number
Δp	[Pa]	pressure drop over ribbed section
Re	-	Reynolds number
T	[K]	temperature
T_∞	[K]	freestream temperature
TKE	[m ² /s ²]	turbulent kinetic energy
t	[s]	time
V	[m ³]	volume
v	[m/s]	velocity
W	[m]	channel width
Δx	[m]	length of ribbed section

Greek symbols

η_T	-	thermal performance
μ	[Pa.s]	dynamic viscosity
ρ	[Kg/m ³]	density

References

- [1] Hagari, T., Ishida, K., Oda, T., Douura, Y., and Kinoshita, Y., 2011, "Heat Transfer and Pressure Losses of W-Shaped Small Ribs at High Reynolds Numbers for Combustor Liner," J. Eng. Gas Turb. Power, 133(9), p. 091901.
- [2] Kunstmann, S., von Wolfersdorf, J., and Ruedel, U., 2010, "Heat Transfer and Pressure Drop in Combustor Cooling Channels with Combinations of Geometrical Elements," ASME Paper No. GT2010-23234.
- [3] Li, Y., Rao, Y., Wang, D., Zhang, P., and Wu, X., 2019, "Heat Transfer and Pressure Loss of Turbulent Flow in Channels with Miniature Structured Ribs on One Wall," Int. J. Heat Mass Transfer, 131, pp. 584-593.
- [4] Maurer, M., von Wolfersdorf, J., and Gritsch, M., 2007, "An Experimental and Numerical Study of Heat Transfer and Pressure Losses of V- and W-Shaped Ribs at High Reynolds Numbers," ASME Paper No. GT2007-27167.
- [5] Zhang, M., Singh, P., and Ekkad, S. V., 2019, "Rib Turbulator Heat Transfer Enhancements at Very High Reynolds Numbers," ASME J. Therm. Sci. Eng. Appl., 11(6), p. 061014.

- [6] Maurer, M., Ruedel, U., Gritsch, M., and von Wolfersdorf, J., 2008, "Experimental Study of Advanced Convective Cooling Techniques for Combustor Liners," ASME Paper No. GT2008-51026.
- [7] Mhetras, S., Han, J. C., and Huth, M., 2014, "Heat Transfer and Pressure Loss Measurements in a Turbulated High Aspect Ratio Channel With Large Reynolds Number Flows," ASME J. Therm. Sci. Eng. Appl., 6(4), p. 041001.
- [8] Rallabandi, A. P., Yang, H., and Han, J. C., 2009, "Heat Transfer and Pressure Drop Correlations for Square Channels with 45 Deg Ribs at High Reynolds Numbers," ASME J. Heat Trans., 131(7), p. 071703.
- [9] Hans, V. S., Saini, R. P., and Saini, J. S., 2010, "Heat Transfer and Friction Factor Correlations for a Solar Air Heater Duct Roughened Artificially with Multiple V-Ribs," Sol. Energy, 84(6), pp. 898-911.
- [10] Ieronymidis, I., Gillespie, D. R. H., Ireland, P. T., and Kingston, R., 2006, "The Use of High Blockage Ribs to Enhance Heat Transfer Coefficient Distributions in a Model of an Integrally Cast Cooling Manifold," ASME Paper No. GT2006-91237.
- [11] Chiang, K. F., Chang, S. W., and Chen, P. H., 2005, "Forced Convective Heat Transfer of 45° Rib-Roughened Fin Flows," Exp. Therm. Fluid. Sci., 29(6), pp. 743-754.
- [12] Tanda, G., 2004, "Heat Transfer in Rectangular Channels with Transverse and V-Shaped Broken Ribs," Int. J. Heat Mass Transfer, 47(2), pp. 229-243.
- [13] Gupta, A., SriHarsha, V., Prabhu, S. V., and Vedula, R. P., 2008, "Local Heat Transfer Distribution in a Square Channel with 90° Continuous, 90° Saw Tooth Profiled and 60° Broken Ribs," Exp. Therm. Fluid. Sci., 32(4), pp. 997-1010.
- [14] Han, J. C., Ou, S., Park, J. S., and Lei, C. K., 1989, "Augmented Heat Transfer in Rectangular Channels of Narrow Aspect Ratios with Rib Turbulators," Int. J. Heat Mass Transfer, 32(9), pp. 1619-1630.
- [15] Kiml, R., Mochizuki, S., and Murata, A., 2001, "Effects of Rib Arrangements on Heat Transfer and Flow Behavior in a Rectangular Rib-Roughened Passage: Application to Cooling of Gas Turbine Blade Trailing Edge," ASME J. Heat Trans., 123(4), pp. 675-681.
- [16] Han, J. C., and Wright, L. M., 2006, "Enhanced Internal Cooling of Turbine Blades and Vanes" in *The Gas Turbine Handbook*, U.S Department of Energy-National Energy Technology Laboratory (NETL), Morgantown, WV, pp. 321-354.
- [17] Han, J. C., Zhang, Y. M., and Lee, C. P., 1991, "Augmented Heat Transfer in Square Channels with Parallel, Crossed, and V-Shaped Angled Ribs," ASME J. Heat Trans., 113(3), pp. 590-596.
- [18] Han, J. C., and Park, J. S., 1988, "Developing Heat Transfer in Rectangular Channels with Rib Turbulators," Int. J. Heat Mass Transfer, 31(1), pp. 183-195.

- [19] Park, J. S., Han, J. C., Huang, Y., Ou, S., and Boyle, R. J., 1992, "Heat Transfer Performance Comparisons of Five Different Rectangular Channels with Parallel Angled Ribs," *Int. J. Heat Mass Transfer*, 35(11), pp. 2891-2903.
- [20] Wright, L. M., Fu, W. L., and Han, J. C., 2004, "Thermal Performance of Angled, V-Shaped, and W-Shaped Rib Turbulators in Rotating Rectangular Cooling Channels (AR=4:1)," *ASME J. Turbomach.*, 126(4), pp. 604-614.
- [21] Han, J. C., and Zhang, Y. M., 1992, "High Performance Heat Transfer Ducts with Parallel Broken and V-Shaped Broken Ribs," *Int. J. Heat Mass Transfer*, 35(2), pp. 513-523.
- [22] Chaube, A., Sahoo, P. K., and Solanki, S. C., 2006, "Analysis of Heat Transfer Augmentation and Flow Characteristics Due to Rib Roughness Over Absorber Plate of a Solar Air Heater," *Renew. Energy*, 31(3), pp. 317-331.
- [23] Lörstad, D., 2011, "LES and RANS Assessment of Rib Cooled Channel Related to SGT-800 Combustor Liner," *ASME Paper No. GT2011-46415*.
- [24] Tang, X. Y., and Zhu, D. S., 2013, "Flow Structure and Heat Transfer in a Narrow Rectangular Channel with Different Discrete Rib Arrays," *Chem. Eng. Process.*, 69, pp. 1-14.
- [25] Abe, K., Kondoh, T., and Nagano, Y., 1994, "A New Turbulence Model for Predicting Fluid Flow and Heat Transfer in Separating and Reattaching Flows—I. Flow Field Calculations," *Int. J. Heat Mass Transfer*, 37(1), pp. 139-151.
- [26] Versteeg, H. K., and Malalasekera, W., 2007, *An Introduction to Computational Fluid Dynamics: the Finite Volume Method*, 2nd ed., Pearson Education Ltd, U.K, pp. 91-92.
- [27] Menter, F. R., 1993, "Zonal Two Equation κ - ω Turbulence Models for Aerodynamic Flows," *AIAA paper Paper No. 93-2906*.
- [28] Ireland, P. T., Neely, A. J., Gillespie, D. R. H., and Robertson, A. J., 1999, "Turbulent Heat Transfer Measurements Using Liquid Crystals," *Int. J. Heat Fluid Flow*, 20(4), pp. 355-367.
- [29] Den Ouden, C., and Hoogendoorn, C. J., 1974, "Local Convective Heat Transfer Coefficients for Jets Impinging on a Plate; Experiments Using a Liquid Crystal Technique," *Proc. of the 5th Int. Heat Transfer Conf.*, Vol. V, New York, pp. 293-297.
- [30] Ireland, P. T., and Jones, T. V., 2000, "Liquid Crystal Measurements of Heat Transfer and Surface Shear Stress," *Meas. Sci. Technol.*, 11(7), pp. 969-986.
- [31] McGilvray, M., and Gillespie, D., 2011, "Transient Heat Transfer Analysis Code for Liquid Crystal Experiments at the University of Oxford: Updated GUI Driven Software," *University of Oxford, Oxford, U.K.*

- [32] Tsang, C. L. P., 2002, "High Blockage Turbulators in Gas Turbine Cooling Passages," Ph.D Dissertation, University of Oxford, Oxford, U.K.
- [33] Clifford, R. J., Jones, T. V., and Dunne, S. T., 1983, "Techniques for Obtaining Detailed Heat Transfer Coefficient Measurements Within Gas Turbine Blade and Vane Cooling Passages," ASME Paper No. 83-GT-58.
- [34] Forsyth, P., McGilvray, M., and Gillespie, D. R. H., 2017, "Secondary Flow and Heat Transfer Coefficient Distributions in the Developing Flow Region of Ribbed Turbine Blade Cooling Passages," *Exp Fluids*, 58(1).
- [35] McGilvray, M., Pineiro, C. O., Axe, T., Ryley, J., and Gillespie, D. R. H., 2013, "Comparison of Stationary Internal Cooling Passage Numerical Simulations to Experimental Data," *Proc. of the 10th European Conf. on Turbomach., Fluid Dyn. and Thermodyn.*, pp. 1-10.
- [36] Ryley, J. R., McGilvray, M., and Gillespie, D., 2019, "Local Heat Transfer Coefficient Measurements on an Engine-Representative Internal Cooling Passage," *J. Thermophys. Heat Transfer*, 33(1), pp. 189-198.
- [37] Byerley, A. R., 1989, "Heat Transfer Near the Entrance to a Film Cooling Hole in a Gas Turbine Blade," Ph.D. dissertation, University of Oxford, Oxford, U.K.
- [38] Moffat, R. J., 1982, "Contributions to the Theory of Single-Sample Uncertainty Analysis," *ASME J. Fluid Eng.*, 104(2), pp. 250-258.
- [39] Çengel, Y. A., 2007, "*Heat and Mass Transfer : A Practical Approach*," 3rd ed., McGraw-Hill, U.S.A, pp. 220-221.
- [40] Bergman, T. L., Lavine, A. S., Incropera, F. P., and DeWitt, D. P., 2011, "*Fundamentals of Heat and Mass Transfer*," 7th ed., Wiley, U.S.A, p. 284.
- [41] Fan, J. F., Ding, W. K., Zhang, J. F., He, Y. L., and Tao, W. Q., 2009, "A Performance Evaluation Plot of Enhanced Heat Transfer Techniques Oriented for Energy-Saving," *Int. J. Heat Mass Transfer*, 52(1-2), pp. 33-44.
- [42] Fiebig, M., 1995, "Embedded Vortices in Internal Flow: Heat Transfer and Pressure Loss Enhancement," *Int. J. Heat Fluid Flow*, 16(5), pp. 376-388.
- [43] Fiebig, M., 1998, "Vortices, Generators and Heat Transfer," *Chem. Eng. Res. Des.*, 76(A2), pp. 108-123.

List of Tables

Table 1: Summary of parameters in investigations pertaining to W type ribs	5
Table 2: Turbulator configurations.....	11

List of Figures

Fig. 1: Schematic representation of experimental facility	7
Fig. 2: Location of instrumented brass rib segments shown by dashed lines	9
Fig. 3: Rib configurations, W (a) and Broken W ribs (b)	10
Fig. 4: Duct configuration (a) turbulator configuration (b) test channel cross section and turbulator height (c).....	11
Fig. 5: Nominal area for HTC averaging (dashed area).....	12
Fig. 6: Numerical domain, shown for the W configuration (a) and the corresponding area (shown by the dashed lines) in the experiment where HTC measurements are compared with the numerically estimated flow structures	16
Fig. 7: Mesh around rib	16
Fig. 8: Normalized HTC contour for W configuration at $Re=903k$ and $P/e=10$	17
Fig. 9: Normalized HTC contour for Broken W configuration at $Re=908k$ and $P/e=10$	17
Fig. 10: Average HTC variation as a function of Reynolds number for the W and Broken W configurations ($P/e=10$)..	18
Fig. 11: Normalized average HTC variation with Reynolds number for the W and Broken W configurations ($P/e=10$) .	19
Fig. 12: Comparison of the heat transfer augmentation variation for the W and Broken W configurations ($P/e=10$) with the literature	19
Fig. 13: Normalized HTC contours for different rib spacings of the Broken W rib configuration	20
Fig. 14: Normalized HTC variation for the Broken W configuration at various rib spacings.....	20
Fig. 15: Normalized friction factor for all four rib configurations investigated	21
Fig. 16: Thermal performance of all four rib configurations investigated	22
Fig. 17: Comparison of thermal performance of W and Broken W configurations at $P/e=10$ with the literature	23
Fig. 18: Rib row numbering	24
Fig. 19: Normalized HTC measured experimentally for the most downstream ribs at $Re=903,000$ (left) and $Re=908,000$ (right), with the 3 zones, shown by dashed boxes, used for the discussion of numerical results	25

Fig. 20: Pathlines on the W configuration (a and b) and Broken W configuration (c and d) with the colors intended for improved visualization..... 25

Fig. 21: Experimental normalized HTC on the most downstream ribbed segments (a & b) and numerically estimated normalized TKE at 0.2xP downstream of the apexes of W and Broken W ribs (c & d) 25